

Electronic Supplementary Information Interfacial Premelting of Ice in Nano Composite Materials

Hailong Li, Markus Bier, Julian Mars, Henning Weiss, Ann-Christin
Dippel, Olof Gutowski, Veijo Honkimäki, and Markus Mezger*

A. Water Bulk Correlations

For water, high precision scattering data were published by Soper and Head-Gordon [1–4]. Figure S1 shows the X-ray scattering intensity $I^{\text{H}_2\text{O}}(q)$ of water at 27 °C. The experimental scattering pattern in the q -range between 0.3 \AA^{-1} and 9.4 \AA^{-1} is perfectly reproduced by a fit of a sum of four pairs of peak functions with width σ_k centered at $\pm q_k$ and a uniform background contribution:

$$I^{\text{H}_2\text{O}}(q) = \sum_{k=1}^4 \left[\frac{A_k(q - q_k) - B_k\sigma_k}{(q - q_k)^2 + \sigma_k^2} - \frac{A_k(q + q_k) + B_k\sigma_k}{(q + q_k)^2 + \sigma_k^2} \right] + C. \quad (\text{S1})$$

Each pair in brackets corresponds to a damped oscillation with periodicity $\lambda_k = 2\pi/q_k$ and decay length $\xi_k = 1/\sigma_k$. The resulting fit parameters are summarized in Table S1. For large distances, correlations with the largest decay length ξ_k dominate. For water the decay modes $k \in \{1, 2\}$ comprise a double-peak of the scattering intensity $I^{\text{H}_2\text{O}}(q)$ at $q_1 = 1.92 \text{ \AA}^{-1}$ and $q_2 = 3.09 \text{ \AA}^{-1}$. Both components, corresponding to the slowest decay of oscillations, exhibit almost the same bulk correlation lengths

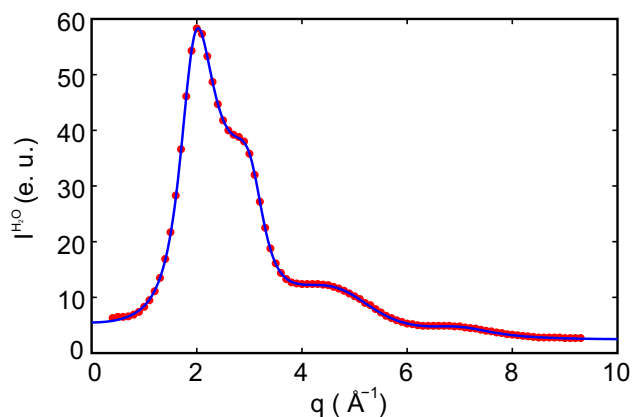


FIG. S1: (color online) Normalized X-ray scattering pattern of bulk water $I^{\text{H}_2\text{O}}(q)$ in electron units (e.u.) at 27 °C (red circles). Data are taken from Hura *et al.*, Table 1 [1]. The solid blue curve is a fit of Eq. (S1) to the experimental data.

TABLE S1: Parameters obtained by fitting Eq. (S1) to water scattering data published by Hura *et al.* [1], see Fig. S1. The background contribution in Eq. (S1) is given by the fit parameter $C = 2.63 \text{ e.u.}$

k	A_k (e.u. \AA^{-1})	B_k (e.u. \AA^{-1})	q_k (\AA^{-1})	σ_k (\AA^{-1})	λ_k (\AA)	ξ_k (\AA)
1	8.25	-17.94	1.92	0.41	3.28	2.43
2	-5.90	-5.79	3.09	0.41	2.03	2.42
3	-5.88	-7.57	4.86	1.16	1.29	0.86
4	-0.08	-1.62	7.00	0.86	0.90	1.16

$\xi_1 \approx \xi_2$. Therefore, $\lambda = \xi = 1/2(\xi_1 + \xi_2) = 2.42 \text{ \AA}$ is used for the bulk correlation length introduced in Eq. (2).

B. Specific Surface Area

Specific surface areas s of vermiculite and kaolin samples were determined from nitrogen adsorption isotherms (Quantachrome, Autosorb 1) at 77.3 K (Fig. S2). Before the measurements, the samples were degassed for 24 h at 130 °C under high vacuum. The isotherms are dominated by the presence of slit mesopores, a very small micropore fraction, but no signs for macropores. Quantitative analysis of the experimental data in the pressure range $0 < p/p_0 < 0.25$ using a BET slit model gave a specific surface area of $s = 36.4 \text{ m}^2/\text{g}$ and $10.9 \text{ m}^2/\text{g}$ for chemically modified vermiculite and kaolin, respectively. For the dried clay minerals, a mass density of $2.63 \text{ g}/\text{cm}^3$ (vermiculite) and $2.70 \text{ g}/\text{cm}^3$ (kaolin) was determined by gas pycnometry (Quantachrome, Ultrapyc 1200e). Thus, the calculated average thickness of the clay platelets L can be estimated to 20.9 nm (vermiculite) and 68.0 nm (kaolin) respectively.

C. Ionic Impurities

The free ion concentration c_i in the clay mineral samples was estimated from electrical conductivity measurements (Greisinger, GLF 100 RW). Approximately 0.5 g dried clay sample was suspended in deionized water (Satorius, Arium611, $18.1 \text{ M}\Omega\text{cm}$). The electric conductivity κ of the suspension was measured after stirring for at least 1 min (Fig. S3). Between subsequent measurements, the water content of the suspension was increased in steps of 10 ml. The free ion concentration in the clay minerals was determined from the relation of κ vs. clay

*Electronic address: mezger@mpip-mainz.mpg.de

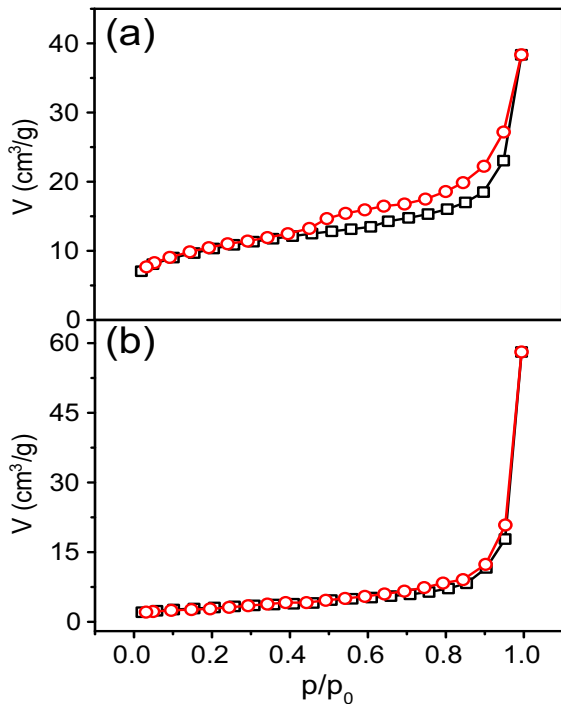


FIG. S2: (color online) Nitrogen adsorption (black squares) and desorption isotherms (red circles) showing the gas volume V vs. relative pressure p/p_0 for (a) vermiculite and (b) kaolin samples.

fraction x using the Debye-Hückel-Onsager equation [5].

$$\kappa = c(\Lambda_0 + K\sqrt{c}) + \kappa_0 \quad (\text{S2})$$

Here $c = c_i x$ is the molar concentration of soluble ions with limiting molar conductivity Λ_0 , $\kappa_0 = 0.65 \mu\text{S}/\text{cm}$ is the measured water conductivity for $x \rightarrow 0$ and $-K = 60.32 + 0.2289 \Lambda_0$. Assuming that the conductivity is entirely caused by K^+Cl^- and NH_4^+Cl^- with limiting molar conductivities $\Lambda_0 = 150 \text{ S cm}^2/\text{mol}$ [5], we obtain a free ion concentration $c_i = 3.8 \mu\text{mol}/\text{g}$ for raw kaolin and $14.5 \mu\text{mol}/\text{g}$ for chemically modified vermiculite. This amounts to a surface concentration of $0.35 \mu\text{mol}/\text{m}^2$ and $0.40 \mu\text{mol}/\text{m}^2$ for kaolin and vermiculite respectively. After subsequent dispersion and filtering cycles of the raw kaolin material in deionized water (P07 sample), the surface concentration was reduced to $0.04 \mu\text{mol}/\text{m}^2$. For the charged vermiculite platelets, the determined ion concentration corresponds to approximately 0.12 free anions per surface unit cell. For comparison, the surface charge per surface unit cell is $1.2 - 1.8$ [6].

D. Scanning Electron Microscopy

The microscopic morphology of the vermiculite and kaolin materials was investigated by scanning electron microscopy (SEM; LEO Gemini 1530; 3 kV acceleration voltage). Figure S4 shows that the powders consist

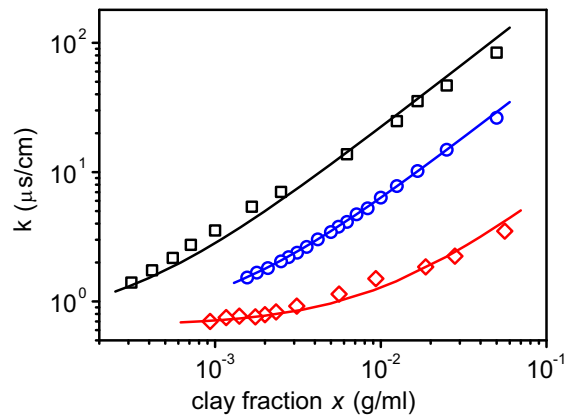


FIG. S3: (color online) Electrical conductivity κ of clay suspensions at different clay fraction; kaolin as received (blue circles), after subsequent dispersion and filtering cycles in deionized water (red diamonds), chemically modified vermiculite (black squares). Solid curves are fits using the Debye-Hückel-Onsager equation (Eq. S2).

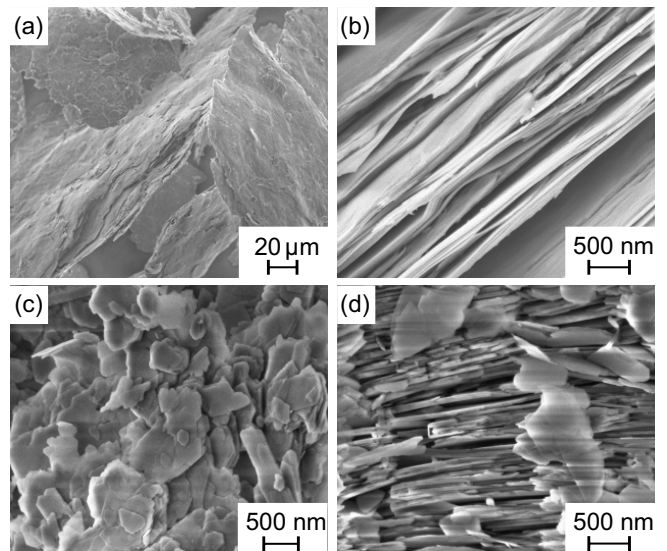


FIG. S4: (color online) SEM image of dry clay platelets; chemically modified vermiculite (a-b), kaolin in top (c) and side view (d). Scale bars represent $20 \mu\text{m}$ (a) and 500 nm (b-d).

of thin platelets high aspect ratio and a lateral length scale in the micrometer regime. They are preferentially stacked parallel to each other. Analysis gives a platelet thickness of approx. 30 nm for vermiculite and 60 nm for kaolin (Fig. S4). These values are in line with estimates L based on the clay surface areas and mass densities (Table 1). Thus, the overall platelet thicknesses are at least one order of magnitude larger than the crystallographic repeat distances of 2.89 nm for vermiculite [7] and 0.739 nm for kaolin sheets silicates [8].

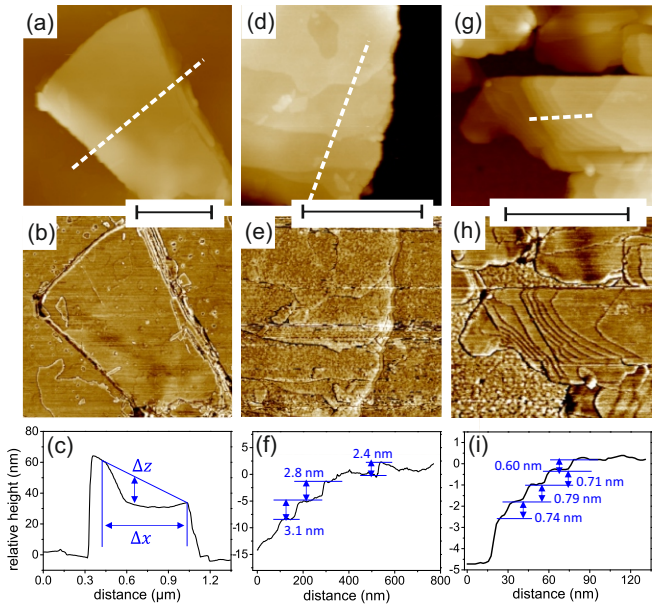


FIG. S5: (color online) AFM images of dry clay platelets; chemically modified vermiculite (a-f), kaolin (g-i), height images (top row), phase images (middle row), height profile along white dash lines (bottom row). Scale bars represent 500 nm (a, b, d, e) and 200 nm (g, h).

E. Atomic Force Microscopy

The surface morphology of the vermiculite and kaolin sheets was investigated by atomic force microscopy (AFM; Dimension icon with ScanAsyst) in tapping mode. AFM images show smooth terraces with step heights around 2.8 nm (vermiculite) and 0.7 nm (kaolin). These step heights correspond to the TOT vermiculite (2.89 nm) [7] and TO kaolin (0.739 nm) [8] smectic layer spacings. For a vermiculite platelet (Fig. S5a), we extract a large radius of curvature $R \approx \frac{\Delta x^2}{2\Delta z} \approx 10 \mu\text{m}$ (Fig. S5c). This confirms that the preparation procedure produces flat, smooth and well defined planar surfaces. Therefore, the premelting model introduced in Sec. 2 provides an adequate description for these clay powders.

F. High Energy X-Ray Diffraction

For experimental parameters see Table S2.

G. XRD Data Processing

Between 1.8 \AA^{-1} and 2.25 \AA^{-1} negative values are observed in the difference patterns (Fig. S7). In this q -range, liquid water shows a strong diffuse scattering signal (red curve) centered around two maxima at 1.92 \AA^{-1} and 3.09 \AA^{-1} (Sec. A). However, extraction of the liquid wa-

TABLE S2: Experimental parameters for the high energy X-ray scattering experiments conducted at ID31, ESRF, Grenoble and P07, PETRA III, Hamburg.

parameter	ID31, ESRF	P07, PETRA III
X-ray energy	71 keV	90 keV
hybride pixel	Dectris PILATUS3	Perkin Elmer
detector	X CdTe 2M	XRD 1621 xN ES
	1478x1679 pixels	2048x2048 pixels
	172 μm pixel size	200 μm pixel size
sample-det. dist.	1660 mm	3300 mm
beam size (h \times v)	0.5 mm \times 0.4 mm	0.5 mm \times 0.5 mm
sample rotation	$\pm 6^\circ$, 0.5° steps	$\pm 6^\circ$, 0.25° steps
	$\pm 2\text{mm}$	$\pm 2.5\text{mm}$
sample transl.	0.5 mm steps	0.25 mm steps
2D datasets	≥ 234	≥ 1920
temp. range	$-60^\circ\text{C} < T < 20^\circ\text{C}$	$-68^\circ\text{C} < T < 2^\circ\text{C}$

ter fraction by direct integration of the diffuse scattering signal with the required accuracy is not possible.

In contrast, the integrated peak intensities of the sharp ice Bragg reflections can be extracted by curve fitting with much higher accuracy. In the fit range between $q = 1.54 \text{ \AA}^{-1}$ and 1.94 \AA^{-1} the smooth scattering signal from liquid water was modeled by a linear background function. For clarity, this linear background was subtracted in the azimuthal integrated difference patterns (Fig. 4). Position q , relative intensity I , and full width of half maximum (FWHM) of ice Ih (100), (002), and (101) Bragg reflections are summarized in Table S3, S4, S5. The CeO_2 (111) Bragg reflection was used for calibration and intensity normalization.

The liquid water fraction $f(T)$ in the partially frozen composite sample is obtained from the normalized Bragg intensities $I(T)$ by assuming full crystallization at -60°C [9].

$$f(T) = 1 - \frac{I(T)}{I(-60^\circ\text{C})} e^{W_D(-60^\circ\text{C}) - W_D(T)}, \quad (\text{S3a})$$

$$\bar{d}(T) = \frac{w_m}{\rho_{\text{H}_2\text{O}} s (1 - w_m)} f(T). \quad (\text{S3b})$$

The exponential function in Eq. (S3a) accounts for the temperature and the q -dependent Debye-Waller factor $W_D(T, q_{hkl})$ of the respective ice (hkl) Bragg reflections [10]. Different intensity ratios of the integrated ice Bragg signals originate from the texture of the confined ice crystals. The ice texture depends on parameters such as the clay surface properties of the clays and cooling rate during crystallization. However, after normalization, for the integrated intensities of all three ice Bragg reflections, the same temperature dependence $f(T)$ was observed (Fig. S8). The effective averaged premelting layer thickness $\bar{d}(T)$ is then calculated using Eq. (S3b). Here, s denotes the specific surface area of the dry clay, w_m the total water weight fraction in the composite samples, and $\rho_{\text{H}_2\text{O}}$ the water mass density.

T [°C]	CeO ₂ (111)		Ice Ih (100)			Ice Ih (002)			Ice Ih (101)		
	q [Å ⁻¹]	FWHM [10 ⁻¹ Å ⁻¹]	q [Å ⁻¹]	FWHM [10 ⁻¹ Å ⁻¹]	I [arb. unit]	q [Å ⁻¹]	FWHM [10 ⁻¹ Å ⁻¹]	I [arb. unit]	q [Å ⁻¹]	FWHM [10 ⁻¹ Å ⁻¹]	I [arb. unit]
-60.0	2.010	1.561	1.605	1.367	3.424	1.709	1.300	1.893	1.819	1.439	1.800
-21.1	2.010	1.560	1.603	1.340	3.265	1.706	1.280	1.816	1.816	1.394	1.688
-16.2	2.009	1.556	1.602	1.330	3.224	1.706	1.266	1.791	1.816	1.382	1.664
-10.4	2.009	1.553	1.602	1.321	3.152	1.705	1.255	1.748	1.815	1.370	1.623
-7.40	2.009	1.550	1.602	1.312	3.088	1.705	1.243	1.709	1.815	1.360	1.591
-5.50	2.009	1.548	1.602	1.305	3.018	1.705	1.234	1.666	1.815	1.351	1.558
-4.00	2.009	1.546	1.602	1.297	2.928	1.705	1.225	1.612	1.814	1.341	1.517
-3.00	2.009	1.544	1.601	1.286	2.812	1.704	1.215	1.545	1.814	1.331	1.465
-2.10	2.009	1.543	1.601	1.275	2.609	1.704	1.202	1.428	1.814	1.318	1.370
-1.10	2.009	1.542	1.601	1.264	2.099	1.704	1.186	1.154	1.814	1.300	1.111
-0.78	2.008	1.541	1.601	1.260	1.727	1.704	1.178	0.958	1.814	1.294	0.921
-0.59	2.008	1.538	1.601	1.256	1.311	1.704	1.172	0.735	1.814	1.290	0.704
-0.40	2.008	1.538	1.601	1.255	0.382	1.704	1.171	0.256	1.814	1.278	0.225

TABLE S3: Fit parameters for vermiculite/ice composites, ESRF, ID31.

T (°C)	CeO ₂ (111)		Ice Ih (100)			Ice Ih (002)			Ice Ih (101)		
	q [Å ⁻¹]	FWHM [10 ⁻¹ Å ⁻¹]	q [Å ⁻¹]	FWHM [10 ⁻¹ Å ⁻¹]	I [arb. unit]	q [Å ⁻¹]	FWHM [10 ⁻¹ Å ⁻¹]	I [arb. unit]	q [Å ⁻¹]	FWHM [10 ⁻¹ Å ⁻¹]	I [arb. unit]
-60.0	2.008	1.564	1.604	1.293	3.241	1.704	1.327	0.498	1.817	1.409	2.088
-29.2	2.008	1.562	1.602	1.275	3.170	1.702	1.316	0.486	1.815	1.389	2.033
-9.60	2.007	1.559	1.601	1.254	3.073	1.701	1.300	0.470	1.813	1.368	1.973
-5.66	2.007	1.557	1.601	1.241	3.005	1.700	1.294	0.461	1.813	1.361	1.937
-2.71	2.007	1.554	1.601	1.225	2.834	1.700	1.280	0.434	1.812	1.347	1.835
-1.23	2.007	1.551	1.601	1.209	2.417	1.700	1.262	0.375	1.812	1.328	1.567
-0.73	2.007	1.547	1.601	1.188	1.885	1.700	1.243	0.295	1.812	1.308	1.228
-0.44	2.007	1.545	1.601	1.177	1.172	1.700	1.230	0.189	1.812	1.296	0.780

TABLE S4: Fit parameters for kaolin/ice composites, ESRF, ID31.

T [°C]	CeO ₂ (111)		Ice Ih (100)			Ice Ih (002)			Ice Ih (101)		
	q [Å ⁻¹]	FWHM [10 ⁻¹ Å ⁻¹]	q [Å ⁻¹]	FWHM [10 ⁻¹ Å ⁻¹]	I [arb. unit]	q [Å ⁻¹]	FWHM [10 ⁻¹ Å ⁻¹]	I [arb. unit]	q [Å ⁻¹]	FWHM [10 ⁻¹ Å ⁻¹]	I [arb. unit]
-68.0	2.010	1.674	1.606	1.628	1.037	1.708	1.507	1.124	1.819	1.621	0.587
-30.0	2.010	1.653	1.604	1.554	0.993	1.706	1.473	1.077	1.817	1.554	0.570
-15.0	2.009	1.683	1.603	1.581	0.977	1.705	1.489	1.052	1.815	1.546	0.542
-10.0	2.009	1.680	1.602	1.583	0.960	1.705	1.482	1.035	1.815	1.533	0.524
-7.00	2.009	1.677	1.602	1.578	0.938	1.705	1.475	1.013	1.814	1.522	0.512
-5.00	2.009	1.677	1.602	1.572	0.901	1.705	1.470	0.982	1.814	1.516	0.495
-3.00	2.009	1.682	1.602	1.555	0.811	1.705	1.454	0.893	1.814	1.495	0.449
-2.00	2.009	1.687	1.602	1.540	0.678	1.704	1.429	0.757	1.814	1.471	0.378
-1.50	2.010	1.658	1.602	1.479	0.556	1.704	1.396	0.615	1.815	1.460	0.329
-1.00	2.010	1.691	1.602	1.461	0.286	1.705	1.387	0.320	1.815	1.503	0.182
-0.80	2.010	1.679	1.602	1.446	0.125	1.704	1.361	0.136	1.815	1.484	0.079
-0.70	2.010	1.676	1.602	1.439	0.052	1.704	1.345	0.053	1.815	1.512	0.033

TABLE S5: Fit parameters for kaolin/ice composites, PETRA III, P07.

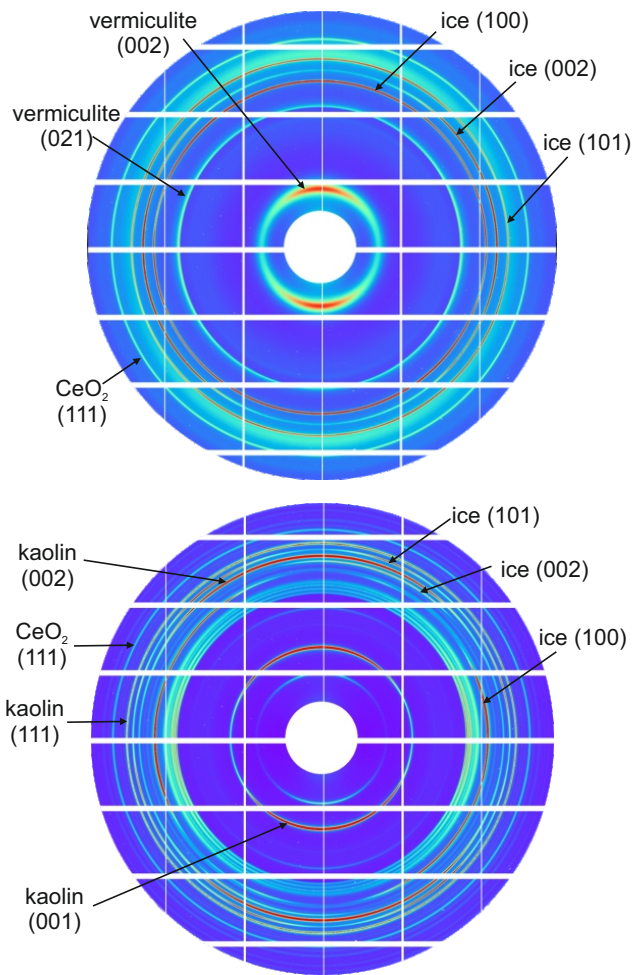


FIG. S6: (color online) 2D-XRD pattern of completely frozen vermiculite/ice (top) and kaolin/ice (ID31, ESRF, bottom) composite at -60°C .

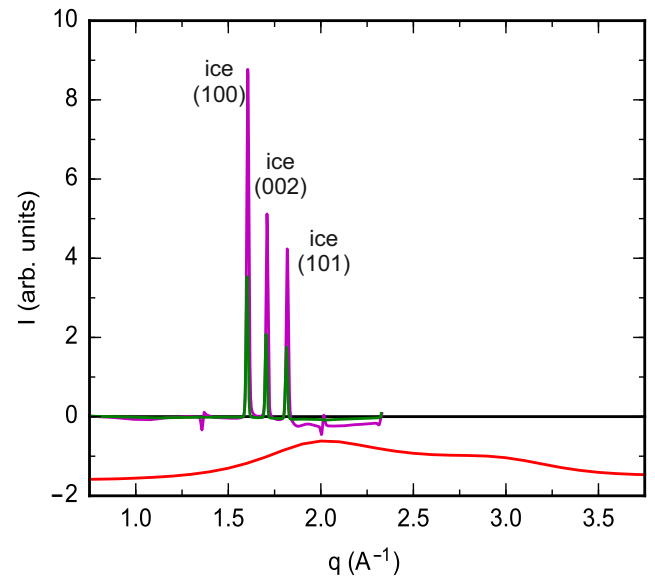


FIG. S7: (color online) Azimuthally integrated XRD difference patterns of partially frozen vermiculite/ice samples at -60°C (purple curve) and -0.59°C (green curve) relative to the molten sample at $+1.1^\circ\text{C}$. The liquid structure factor of liquid water taken from Hura et al. [1] is shown for comparison (red curve, scaled and shifted vertically for clarity).

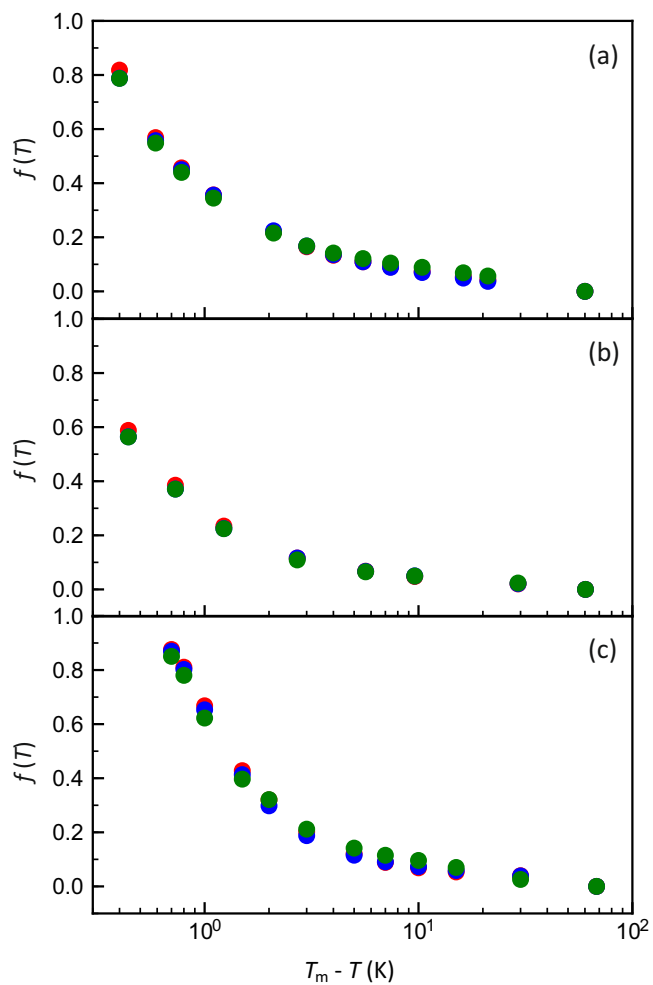


FIG. S8: (color online) Liquid water fraction $f(T)$ in clay composites determined from the intensity of the (100) (red), (002) (blue), (101) (green) ice Ih Bragg reflections; (a) vermiculite, (b) kaolin ESRF, ID31 data, (c) kaolin PETRA III, P07 data.

-
- [1] G. Hura, J. M. Sorenson, R. M. Glaeser and T. Head-Gordon, *J. Chem. Phys.*, 2000, **113**, 9140–9148.
- [2] A. Soper, *Chemical Physics*, 2000, **258**, 121–137.
- [3] T. Head-Gordon and G. Hura, *Chem. Rev.*, 2002, **102**, 2651–2670.
- [4] A. Soper, *J. Phys. Condens. Matter*, 2007, **19**, 335206.
- [5] D. W. Ball, *Physical chemistry*, Thomson-Brooks/Cole, Pacific Grove CA, 2003.
- [6] I. Bihannic, A. Delville, B. Demé, M. Plazanet, F. Villiéras and L. J. Michot, in *Clay Swelling: New Insights from Neutron-Based Techniques*, ed. L. Liang, R. Rinaldi and H. Schober, Springer, New York, 2009, pp. 521–546.
- [7] A. M. Mathieson and G. Walker, *Am. Mineral.*, 1954, **39**, 231–255.
- [8] D. L. Bish, *Clays Clay Miner*, 1993, **41**, 738–744.
- [9] S. Engemann, H. Reichert, H. Dosch, J. Bilgram, V. Honkimäki and A. Snigirev, *Phys. Rev. Lett.*, 2004, **92**, 205701.
- [10] B. Wehinger, C. Dmitry, K. Michael, B. Sergey, E. Victor and B. Alexei, *J. Phys.: Condens. Matter*, 2014, **26**, 265401.